

Seed-Crystal-Induced Cold Sintering Toward Metal Halide Transparent Ceramic Scintillators

Journal Article

Author(s):

Han, Kai; [Sakhatskyi, Kostiantyn](#) ; Jin, Jiance; Zhang, Qinyuan; Kovalenko, Maksym V.; Xia, Zhiguo

Publication date:

2022-04-27

Permanent link:

<https://doi.org/10.3929/ethz-b-000541609>

Rights / license:

[In Copyright - Non-Commercial Use Permitted](#)

Originally published in:

Advanced Materials 34(17), <https://doi.org/10.1002/adma.202110420>

Metal halides transparent ceramic scintillators for high-spatial resolution and low-dose X-ray imaging

Kai Han¹, Kostiantyn Sakhatskyi^{2, 3}, Jiance Jin¹, Qinyuan Zhang^{1,4}, Maksym V. Kovalenko^{2, 3}, Zhiguo Xia^{1, 4*}

¹State Key Laboratory of Luminescent Materials and Devices and Institute of Optical Communication Materials, Guangdong Provincial Key Laboratory of Fiber Laser Materials and Applied Techniques, School of Materials Science and Engineering, South China University of Technology, Guangzhou, 510641, China

²Department of Chemistry and Applied Biosciences, Institute of Inorganic Chemistry, ETH Zürich, 8093 Zürich, Switzerland.

³Empa-Swiss Federal Laboratories for Materials Science and Technology, 8600 Dübendorf, Switzerland.

⁴School of Physics and Optoelectronics, South China University of Technology, Guangzhou, Guangdong, 510641, China.

Scintillators with high spatial resolution at a low radiation dose rate are desirable for X-ray medical imaging. To challenge the state-of-art technology, it is necessary to simultaneously achieve the high light yield, oriented light transport, and reduced light scattering, all with large-area, inexpensive fabrication methods. Here, we fabricated <001>-textured $\text{TPP}_2\text{MnBr}_4$ (TPP: tetraphenylphosphonium) ceramic scintillator by a facile seed-crystal induced cold sintering process, with large-area wafer of 5 cm in diameter exhibiting high optical transparency of above 68 % over 450-600 nm range. Compelling scintillation performance includes light yield of $ca. 78000 \pm 2000$ photons per MeV, low detection limit 8.8 nanograys per second, about 625 times slower than the requirement of X-ray diagnostics (5500 nanograys per second), and energy resolution of 17% for high-energy γ -rays (662 keV). X-ray imaging with as-prepared samples demonstrated a high spatial resolution of 15.7 lp mm^{-1} . Moreover, the designed material exhibits good retention of the radioluminescence intensity and light yield, with the drop of less than 12 % over a wide temperature range of 20-160 °C, good cycling reliability up to 10^6 cycles with moderate property degradation (under 9 %), and minimal variations (< 2 %) at high temperature (85 °C) and high humidity atmosphere (85%) system. This work presented a paradigm for achieving light-guiding property with high transparency and large-area fabrication by grain orientation engineering, and we expect the transparent, textured metal halide ceramic scintillator reported here to provide a route for advancement in the X-ray imaging field.

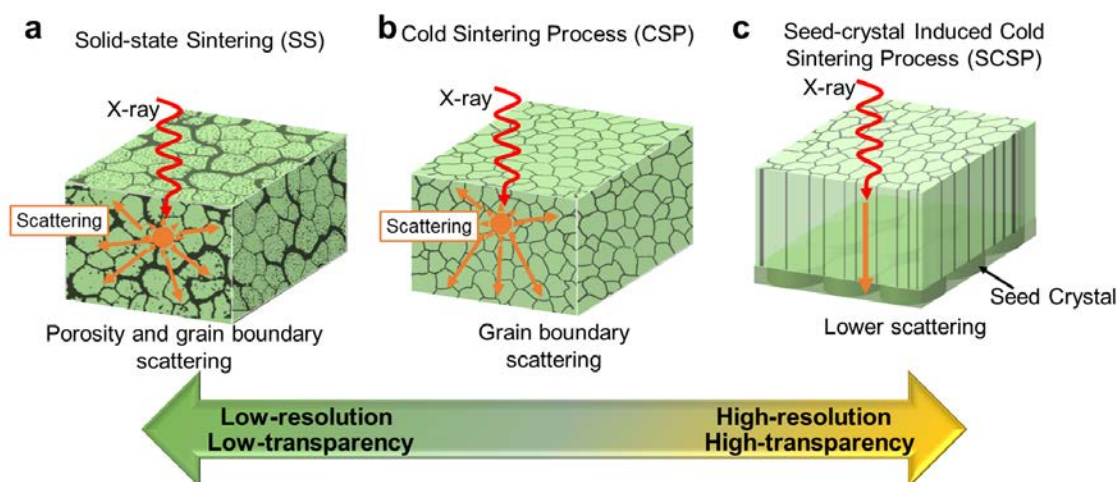
X-ray detectors based either on the indirect conversion or direct conversion methods are broadly used in security, medical imaging, industrial material inspection, and nuclear power stations.¹⁻⁴ The mainstream indirect-conversion method utilizes a scintillator to firstly convert X-ray to light and subsequently convert light to electronic signals by a photodetector.⁵ Recent years faced growing interest to metal halide scintillators (MHS), such as $\text{Cs}_3\text{Cu}_2\text{I}_5$, Rb_2CuBr_3 , $\text{Cs}_2\text{Ag}_{0.6}\text{Na}_{0.4}\text{InCl}_6$, and $(\text{C}_{38}\text{H}_{34}\text{P}_2)\text{MnBr}_4$.⁶ These scintillation crystals possess very high light yield (LY ~ 39000 to 91000 photons per MeV),⁷⁻¹¹ comparing favorably to conventional scintillators such as CsI(Tl) , LuAG:Ce and LYSO:Ce single crystals with LY of 25000 to 54000 photons per MeV. MHS crystals can be grown by solution methods, which is the advantage over the high-temperature crystal growth.^{7,12} The main drawbacks of the solution-growth lie in the difficulty of growing sufficiently large crystals and poor control over the directionality of growth.

Aiming to match specific requirements of different applications, various forms of MHS materials were explored: i.e., nanocrystal thin films,^{1,7} colloiddally dispersed nanocrystals,¹³ organic composite film (such as a mixture of MHS and polydimethylsiloxane),¹⁰ and wafers.¹³ However, the former two approaches are limited by either the small emission Stokes shift (halide perovskites) or have limited durability. The

latter two methods suffer from poor optical transparency caused by light scattering on pores and grain boundary, as shown in Scheme 1a, thus, resulting in reduced X-ray imaging spatial resolution, as observed in $\text{Cs}_2\text{Ag}_{0.6}\text{Na}_{0.4}\text{In}_{0.85}\text{Bi}_{0.15}\text{Cl}_6$ and $\text{C}_6\text{H}_{12}\text{NMnCl}_3$ wafers.^{13,14} Recently, Eu^{3+} doped CsPbBr_3 glass-ceramic, with good optical homogeneity, realized a high spatial resolution of 15.0 lp mm^{-1} , yet along with decreased light yield of 10100 photons per MeV.¹⁵ It thus remains a formidable challenge with MHS to achieve a compelling combination of optical transparency and high light yield using scalable and inexpensive fabrication methods.

Transparent polycrystalline ceramics has emerged as a cost-effective material in X-ray imaging for excellent optical transparency.¹⁶ Moreover, these ceramics usually possessing a reduced density of grain boundaries, and the absence of pores are prepared by the state-of-the-art sintering process such as hot-pressing sintering, microwave sintering, and spark plasma sintering, during which starting powders with high purity are involved.^{12,17-20} Nevertheless, the hot heat sintering process is inadequate to be applied to low-melting metal halides. A spick-and-span technique, thus, is imperative for transparent ceramic-based MHS, to enable lowering sintering temperature. In this respect, the cold sintering process (CSP, sintering temperature

Scheme 1 Schematic diagram of grain structures in ceramics based on various methods. a Light scattering of residual porosity in conventional solid-state sintering. **b** Light scattering of grain boundary in the traditional cold sintering process. **c** No light scattering as light travels through homogeneous grain ceramics formed by seed-crystal induced cold sintering process.



≤ 300 °C normally), as liquid phase sintering process, could provide a densification environment compatible with low-melting metal halide.²¹ Traditional CSP might upgrade crystal light scattering within the crystalline phase owing to anisotropic grain and grain boundary, as demonstrated in Scheme 1b. For reducing the grain boundaries, grain engineering is employed. Since the dissolution precipitation process in CSP with templated seed induced grain-growth approach, the templated seed can be employed during the dissolution precipitation process in CSP, which concurrently minimizes the surface free energy while removing porosity, as shown in Scheme 1c.

In this work, we developed a facile seed-crystal-induced cold sintering process (SCSP) that allows us to fabricate transparent ceramic-based MHS directly (Scheme 1c). The approach is showcased with the zero-dimensional (0D) organic-inorganic hybrid halide $\text{TPP}_2\text{MnBr}_4$ (TPP: tetraphenylphosphonium). This compound has a high photoluminescence quantum yield of 98%, but is difficult to prepare as large crystals.¹⁰ The high-quality $\langle 001 \rangle$ -textured $\text{TPP}_2\text{MnBr}_4$ ceramic scintillators were fabricated, with homogeneous crystalline size and uniform orientation of the grains. As expected, the grain boundary density at $\langle 001 \rangle$ orientation is lowered substantially, leading to improved transparency (over 68 %, ranging from 450 to 600 nm) and scintillation performance (high light yield $\sim 78000 \pm 2000$ photons per MeV, low detection limit 8.8 nanograys per second and energy resolution of 17% for 662 keV) at a large-area wafer of 5 cm diameter. A high spatial resolution of 15.7 lp mm^{-1} was observed in $\text{TPP}_2\text{MnBr}_4$ X-ray scintillation imaging. The material exhibits high radioluminescent stability of radioluminescence intensity and light yield (< 12 %) over a wide temperature range of 20-160 °C, excellent cycling reliability up to 10^6 cycles (< 9 %), and minimal variations (< 2 %) at high temperature (85 °C) and high humidity atmosphere (85%) system. The innovative synthetic process for transparent metal halide ceramics demonstrated here is expected to be of general utility for metal halides and other structurally soft

materials for their deployment in X-ray imaging device applications.

RESULTS

Structure and photoluminescence properties of $\text{TPP}_2\text{MnBr}_4$. We obtained $\text{TPP}_2\text{MnBr}_4$ crystals using solvent-antisolvent recrystallization, i.e., diffusing diethyl ether into a N,N-dimethylformamide (DMF) precursor solution containing TPPBr and MnBr_2 with a mole ratio of 2:1. The crystal structure of $\text{TPP}_2\text{MnBr}_4$ single crystals with a monoclinic space group of $C2/c$ was shown in Figure 1a and Supplementary Table 1, in which isolated $[\text{MnBr}_4]^{2-}$ tetrahedrons were surrounded by TPP^+ cations. A significant Mn-Mn distance (shortest distances: 10.38 Å), thanks to a large and bulky TPP^+ cation, reduces the energy transfer between the Mn ions and hence the quenching of the PL by symmetry-directed spin-exchange interactions and dipole-dipole interactions.²²⁻²⁴ The powder X-ray diffraction (PXRD) pattern of as-prepared materials is in agreement with the simulated consequence from single-crystal diffraction (SCXRD) data (Supplementary Figure 1), confirming the high phase purity of the $\text{TPP}_2\text{MnBr}_4$ single crystals.

The photoluminescence excitation (PLE) spectroscopy of $\text{TPP}_2\text{MnBr}_4$ shows two intense bands excitation peaks at 360 and 450 nm from two energy transitions: $^6\text{A}_1 \rightarrow ^4\text{G}$ (430-480 nm) and $^6\text{A}_1 \rightarrow ^4\text{D}$ (350-390 nm) on the basis of crystal-field models through the Tanabe-Sugano diagram (Figure 1b and Supplementary Table 2).²⁵ The $\text{TPP}_2\text{MnBr}_4$ displays intensive green photoluminescence (PL) with a featureless emission band centered at 520 nm and a full width at half-maximum (fwhm) of 42 nm, owing to the $^4\text{T}_1 \rightarrow ^6\text{A}_1$ transition of the Mn (II) ion in d^5 configuration. A high photoluminescence quantum yield (PLQY $\sim 98\%$) was recorded.^{22,26} The aforementioned features-single crystals, high purity raw materials, and high PLQY- play an essential role in achieving high transparency metal halide scintillant ceramics.

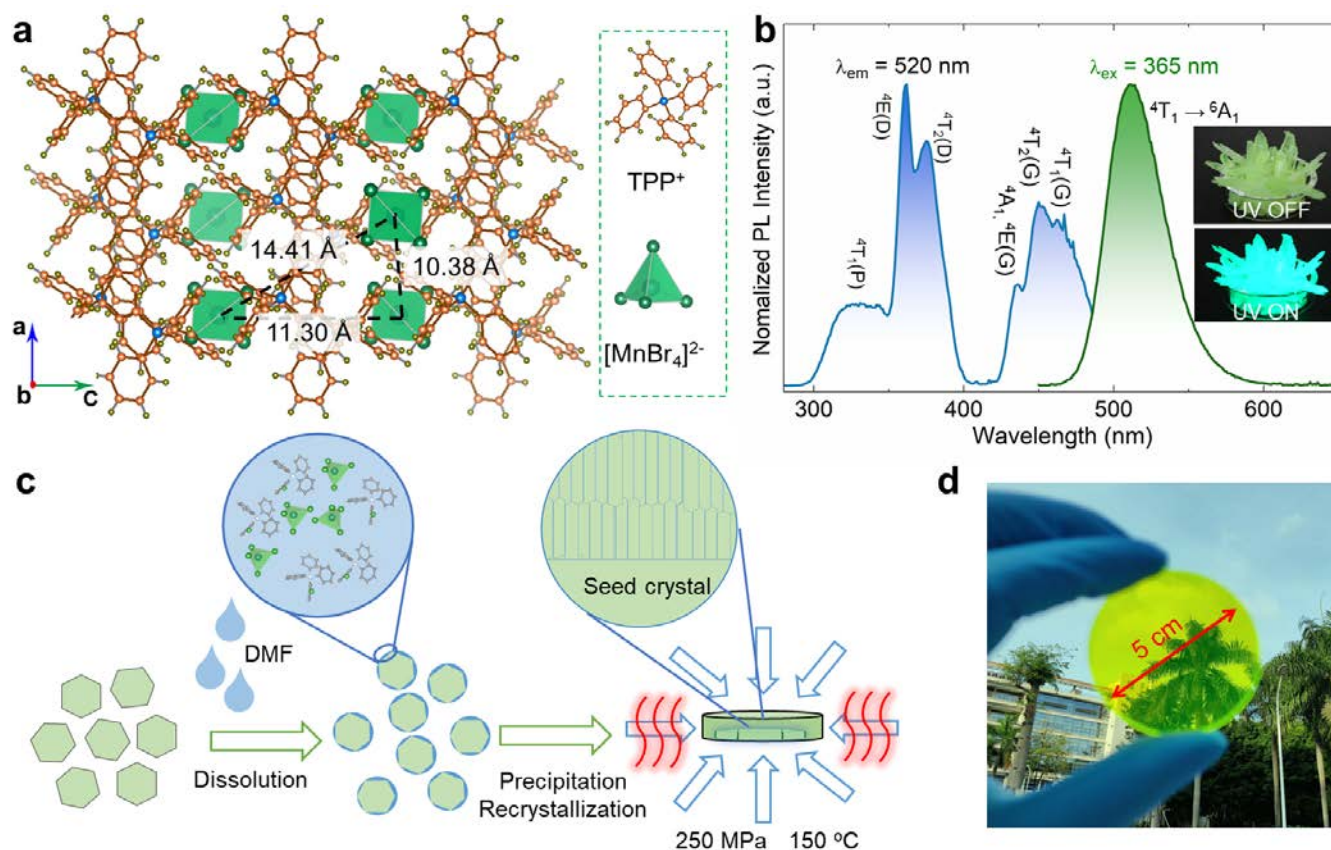


Figure 1 Crystal Structure and photoluminescence properties of TPP₂MnBr₄, fabrication textured TPP₂MnBr₄ ceramic scintillator. **a** Structure of 0D TPP₂MnBr₄ (green tetrahedrons: [MnBr₄]²⁻ tetrahedrons). **b** Excitation (PLE), and emission (PL) spectra of TPP₂MnBr₄, the insets are photographs of TPP₂MnBr₄ columnar single crystals under ambient light and UV light (365 nm). **c** Fabrication process via seed-crystal induced cold sintering process. **d** Photographs of textured TPP₂MnBr₄ ceramic scintillator with thicknesses of 1 mm under ambient light.

Seed-crystal induced cold sintering process. In the search for suitable scintillation luminophores and the preparation method of large-area scintillation ceramics with high transparency, we picked out <001>-orientation cylinder growing TPP₂MnBr₄ single crystals as the seed-crystal, where <001>-orientation was confirmed by preferred (001) peaks (Supplementary Figure 2). Accordingly, such a seed-crystal-induced cold sintering process is proposed, in view of grain orientation engineering, low melting, and <001>-orientation-growing columnar single crystals characteristics of TPP₂MnBr₄. This is, SCSP diminishes residual porosity content, while seed-crystal induced unique <001>-orientation growth decreases grain boundary density, collectively contributing to high transparency textured ceramics. The fabrication method of dense TPP₂MnBr₄ textured ceramics is shown in Figure 1c. To obtain a homogeneous structure, high purity TPP₂MnBr₄ raw powders was mixed with 20-40 wt% DMF solution to dissolve particle surface. Afterward, <001>-orientation templates, fabricated by shearing TPP₂MnBr₄ columnar single crystals, was added into the mold with raw powders homogeneously. Finally, the wetted powders were pressed in a die under a pressure of 250 MPa at a temperature of 150 °C for 2-24 h. More details can be found in the Experimental Section. At this stage, grain surface and small grains are dissolved in DMF, followed by grain rearrangement and recrystallization introduced by <001>-orientation seed-crystal. As the number of <001>-orientation grains could form via dissolution-

recrystallization. As demonstrated in Supplementary Figure 3, remarkably enhanced relative densities above 98 % are observed with the increase of sintering time, showing that SCSP is a promising technique to fabricate metal halide composite materials. Thanks to the above-mentioned process, a transparent centimeter-scale (5 cm diameter, 1 mm thickness) textured ceramic-based scintillator wafer is obtained and shown in Figure 1d.

Microstructure of textured TPP₂MnBr₄ ceramic scintillator. To recognize the underlying formation mechanisms responsible for the perfect transparency and light transmission property, the micro-morphology of lateral and top surfaces was studied. The textured ceramics unfold highly compacted grains with nearly pore-free microstructure, consistent with a high relative bulk density of >98 %, by virtue of SCSP with high temperature and pressure. Interestingly, the ordered and clubbed grains along the seed crystal direction could be found in Figure 2a, further confirmed by quasi square grain topography in the top-view (Figure 2b). The X-ray diffraction (XRD) data of the bulk surfaces and powders was shown in Supplementary Figure 4, in which bulk surfaces exhibit greatly enhanced intensities of the (001) peaks, further demonstrating a remarkable arrangement of grains. The Lotgering factor F_{001} of the textured ceramics is up to 91%, revealing a pronounced <001>-preferred orientation degree of crystalline texture. Electron backscatter diffraction (EBSD) (Figure 2c) and (001) pole figures (Figure 2d) measurements

corroborate that the $\langle 001 \rangle$ -oriented grains preferred to grow on account of $\langle 001 \rangle$ -preferred seed crystal.²⁷⁻²⁹ These observations mentioned above provide strong shreds of evidence that seed crystal introducing grain engineering prefers $\langle 001 \rangle$ orientation grain growth. Moreover, these clubbed grains in the textured ceramics help to the formation of the waveguide structure that can guide light effectively from the bottom to the top surface, while nothing can be found from the lateral surface (Figure 2e).³⁰ And it is also beneficial to the

scintillation performance since the emitted light is guided along the ordered and clubbed grains. Furthermore, the textured poled samples at top surface direction exhibited enhanced linear transmittance for the visible-light spectrum compared to the one at lateral surface direction (Figure 2f), which strongly verifies the waveguide structure, and thus most of the incident X-rays are converted to scintillation lights, as verified by the excellent scintillation performance.

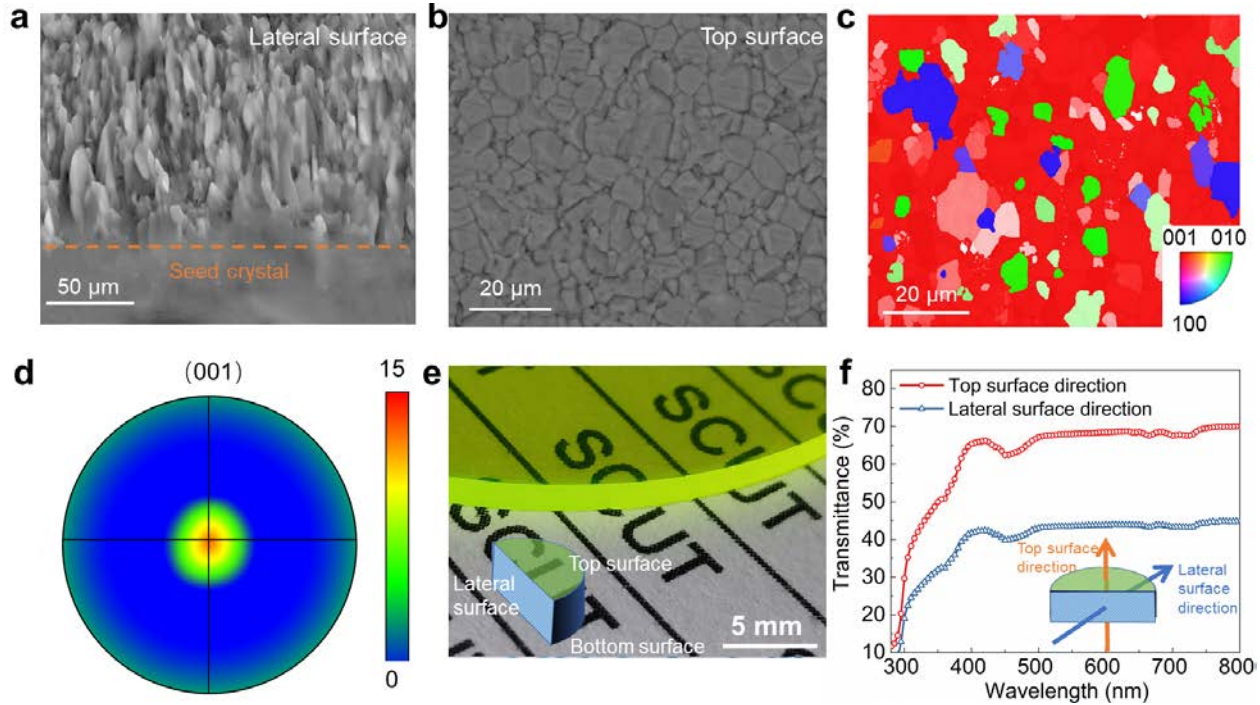


Figure 2 Microstructure and texture quality of textured $\text{TPP}_2\text{MnBr}_4$ ceramic scintillator. **a** SEM image of the lateral fracture surface of $\langle 001 \rangle$ -textured $\text{TPP}_2\text{MnBr}_4$ ceramic scintillator. **b** SEM image of the top surface of $\langle 001 \rangle$ -textured $\text{TPP}_2\text{MnBr}_4$ ceramic scintillator. **c** Grain orientations for the $\langle 001 \rangle$ -textured $\text{TPP}_2\text{MnBr}_4$ ceramic scintillator measured by the SEM-EBSD technique. **d** The (001) pole figures of textured $\text{TPP}_2\text{MnBr}_4$ ceramic scintillator. **e** Diagonal view of the polished $\text{TPP}_2\text{MnBr}_4$ ceramic scintillator with thicknesses of 1 mm under ambient light. **f** Light transmittance along top and lateral surface direction of $\langle 001 \rangle$ -textured $\text{TPP}_2\text{MnBr}_4$ ceramic scintillator.

Scintillation performance of textured $\text{TPP}_2\text{MnBr}_4$ ceramic scintillator. To investigate the impact of grain orientation engineering on scintillation performance, we fabricated three bulk materials by SS, CSP and SCSP with the same size as shown in the insets of Figure 3a. The light transmittance in the visible light range of the SCSP sample is much higher than those of the CS and SS samples (Figure 3a). The weakened light transmittance for CSP and SS samples is attributed to random and loose micro-morphology and no-textured structure (Scheme 1 and Supplementary Figure 5). In terms of the scintillation performance, we firstly calculated the absorption coefficient and X-ray attenuation efficiency for the $\text{TPP}_2\text{MnBr}_4$ and the typical scintillators (LuAG:Ce and CsI(Tl) as reference samples) to allow a favorable thickness to be used to evaluate the scintillation performance of $\text{TPP}_2\text{MnBr}_4$ (Supplementary Figure 6). The SCSP, CSP, and SS samples show bright green X-ray radioluminescence (RL) under X-ray excitation (Supplementary Figure 7). Of particular importance is that the SCSP with high transparency exhibits greatly intense RL contrasted to CS and SS, owing to lower light scattering in bulk materials. The light yield (LY) of a scintillator, namely the X-ray-to-photon conversion efficiency, can be measured by the

ratio of the total emitted photon number of $\text{TPP}_2\text{MnBr}_4$ and reference sample at equivalent absorbed X-ray energy. In this work, a commercial LuAG:Ce scintillator (25000 photons per MeV) was selected as a reference. As a result, the SCSP, CSP, and SS samples deliver light yields of 78000 ± 2000 , 69000 ± 3000 , and 64000 ± 2000 photons per MeV, respectively (Figure 3b). Benefitted from brighter RL, the SCS counterpart displayed the linear response range to X-ray dose rate (Supplementary Figure 8b), realizing lower the detection limit 8.8 nanograys per second derived (Figure 3b) from the fitting curve when the SNR equals 3, which is about 625 times lower than the requirement of X-ray diagnostics (5.5 micrograys per second).⁹ It should be noted that the SCSP counterpart exhibits more attractive scintillation performance with both higher light yield and lower detection limit compared with state-of-the-art scintillators (Supplementary Figure 9).

To further prove the utility of SCSP as a scintillator for practical X-ray imaging, a self-made optical system was constructed, in which an X-ray source, the imaging object, textured ceramics and a smartphone camera was placed in sequence, as illustrated in Figure 3c. X-ray images of a circuit board with clear electric circuit were successfully acquired by

using SCSP, CSP, and SS as scintillators. As expected, the clearly better image is observed in SCSP scintillator screen compared with CSP and SS, owing to the decreasing light scattering and improved RL (Figure 3f), as discussed formerly. The modulation transfer functions (MTF) of images obtained from SCSP, CSP, and SS scintillator screen, as plotted in Figure 3d, have been employed to further evaluate image quality based on X-ray edge images (insets of Figure 3d). As the spatial frequency (lp mm⁻¹) at MTF = 0.2, the spatial resolution of SCS

is acquired as 15.7 lp mm⁻¹, which is much larger than 12.0 lp mm⁻¹ for CS and 7.2 lp mm⁻¹ for SS scintillator screens. And it is even superior to 10 lp mm⁻¹ of X-ray imaging for commercial CsI(Tl) scintillator and direct X-ray detectors (Cs₂AgBiBr₆ and MAPbBr₃), as shown in Figure 3e.³¹⁻³³ All the above-mentioned merits of SCSP demonstrate that high transparency textured ceramics constructed by grain engineering is more promising scintillator.

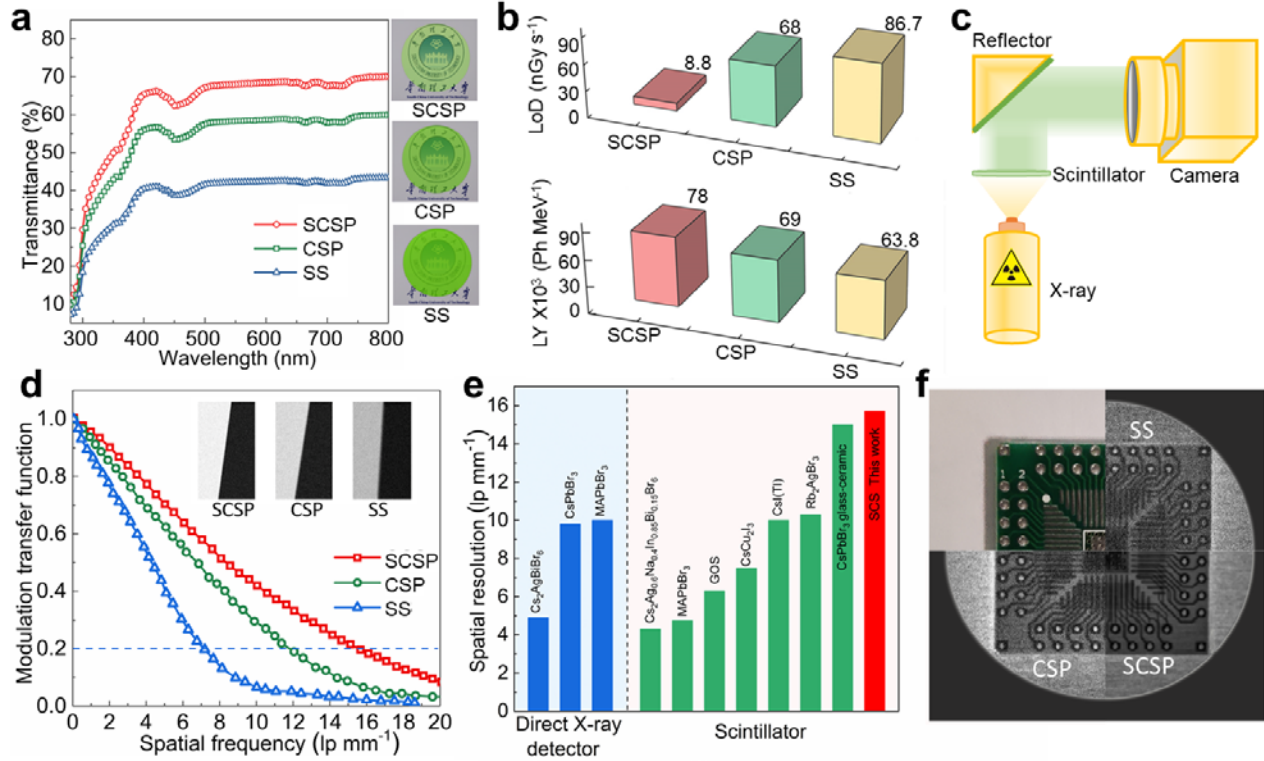


Figure 3 Scintillation performance of textured TPP₂MnBr₄ ceramic scintillator. **a** Light transmittance of SCS, CS, and SS with thicknesses of 0.5 mm. **b** Light yield and detection limit of SCS, CS, and SS. **c** Schematic of X-ray imaging system. **d** Modulation transfer functions (MTF) of X-ray images obtained from SCS, CS, and SS. **e** Comparison of spatial resolutions in representative scintillators and direct X-ray detectors.^{1,9,11,15,31-36} **f** Photograph and X-ray images of circuit board using SCS, CS, and SS.

Additionally, we were able to demonstrate with SCSP scintillator a single-photon γ -ray counting ability and subsequently, energy-resolved γ -ray spectra (Supplementary Figure 10), which potentially may find application in the X-ray spectral imaging.³⁷ The clear single-photon traces are obtained with SCS coupled with photomultiplier tube under irradiation of isotope sources Cs¹³⁷ (Supplementary Figure 10a) and Am²⁴¹ (Supplementary Figure 10b). Pulse amplitude distributions (*i.e.* energy spectra) from corresponding sources were collected (Supplementary Figure 10c,b) with the multichannel analyzer after processing with the shaping amplifier. Photopeak, corresponding to full γ -photon absorption, is observed on each energy spectra. We estimate the energy resolution, which is defined as a ratio of a full width on half-max on photopeak energy, for Cs¹³⁷ (γ -ray energy 662 keV) 17% and for Am²⁴¹ (γ -ray energy 60 keV) 40%, which is compatible to state-of-art scintillator materials.^{38,39} In addition, we measured with the same scheme the energy-resolved α -particle spectra from open Am²⁴¹ source with energy resolution 22% (Supplementary Figure 11).

For practical scintillation applications, X-ray imaging and operation stability, including cycling reliability, and

temperature and humidity stability is important. The cycling reliability of scintillation performance of SCS is evaluated at dose rate of $\sim 50 \mu\text{Gy}_{\text{air}} \text{s}^{-1}$, the corresponding results are given in Supplementary Figure 12a. The SCS exhibits outstanding RL intensity and LY cycling reliability after 10⁶ cycles, with variations of $< 9\%$. Temperature and humidity stability the safety in practical application, lowering the possibility of release of radiation. The temperature-dependent scintillation property of SCS over the temperature range of 20-160 °C is estimated (Supplementary Figure 12b and Supplementary Figure 13). RL intensity and LY degradations are $< 12\%$. Both RL intensity and LY maintain minimal variations ($< 2\%$) at high temperature (85 °C) and high humidity atmosphere (85%) system, indicating the SCS has outstanding humidity stability. The scintillation stability is associated with larger Mn-Mn distance and stronger ionic bonding Mn cations and Br ions, which could be supported by higher binding energies for Mn2p and Br3d (Supplementary Figure 14).⁴⁰ To further demonstrate the practical X-ray imaging, Supplementary Figure 15a shows the X-ray images of the circuit board, revealing the detailed structural information on a transistor panel under a resin cover. Biological tissue phase such as crab can also be recorded

(Supplementary Figure 15b) and shows high-quality X-ray images. Furthermore, the X-ray imaging of biological tissues was successfully recorded, in which muscle tissue, skeleton, cataclasis, and inserted needle were clearly visible at low dose rate of $\sim 2 \mu\text{Gy}_{\text{air}} \text{ s}^{-1}$, (Supplementary Figure 16).

Conclusion

In summary, we developed a facile grain orientation engineering strategy to fabricate a novel metal halide transparent ceramic scintillator by a seed-crystal induced cold sintering progress. Large-area fabrication (wafer of 5 cm diameter) and high transparency (over 68 %, ranging from 450 to 600 nm) have been realized in <001>-textured $\text{TPP}_2\text{MnBr}_4$ ceramic scintillator. An ultrahigh light yields of 78000 ± 2000 photons per MeV, a low detection limit of 8.8 nanograys per second, an energy resolution of 17% for high-energy γ -rays (662 keV) and a high-resolution X-ray imaging of 15.7 lp mm^{-1} were achieved. More importantly, the material exhibits good fatigue endurance and temperature humidity stability, variations of RL intensity and LY < 9 %, 12%, and 2% for 10^6 cycles, temperature range of 20-160 °C system, respectively. All the merits demonstrate that grain orientation engineering opens an exciting pathway for the fabrication of large-area perfect transparent textured ceramics, and the newly discovered <001>-textured $\text{TPP}_2\text{MnBr}_4$ ceramic scintillator will work as a promising candidate for high-resolution scintillation applications.

Methods

Materials. Tetraphenylphosphonium bromide (TPPBr, 99.5%), manganese bromide tetrahydrate ($\text{MnBr}_2 \cdot 4\text{H}_2\text{O}$, 99.9%), *N,N*-dimethylformamide (DMF, 99.5%), and ethyl ether ($\text{C}_4\text{H}_{10}\text{O}$, 99.7%) were all purchased from Sigma-Aldrich. $\text{MnBr}_2 \cdot 4\text{H}_2\text{O}$ be heated at 120 °C for 24 h to remove the crystal water. All the chemicals were used without further treatment.

Growth of $\text{TPP}_2\text{MnBr}_4$ Single Crystals. The $\text{TPP}_2\text{MnBr}_4$ single crystals were grown by an antisolvent method. Specifically, TPPBr (0.8386 g, 2 mmol) and MnBr_2 (0.2147 g, 1 mmol) were first dissolved in DMF (2 mL) solution filtered into a 10 mL glass vial to form a clear precursor solution. Then, the vial was placed in a sealed 50 mL vial with 10 mL Et_2O inside. A large number of green column crystals would be produced. Then the as- prepared crystals were washed by Et_2O , and dried overnight at 60 °C.

Fabrication of $\text{TPP}_2\text{MnBr}_4$ Ceramic Scintillators. The $\text{TPP}_2\text{MnBr}_4$ powders were mixed with 13-25 wt % DMF solution. Specifically, 0.13-0.25 g DMF solution was added into 1 g $\text{TPP}_2\text{MnBr}_4$ powders and homogenized with a pestle and mortar for several minutes. The wetted powders and <001>-orientation seed crystals were placed in a steel die with a diameter of 50 mm. Then, the die under pressure of 250 MPa was heated up to 150 °C with a ramp of $10 \text{ }^\circ\text{C min}^{-1}$, and held at 150 °C for 6-48 h. Afterward, the die was cooled down in air and the samples were taken out after the temperature was lower room temperature.

Single-crystal X-ray diffraction. Single-crystal X-ray diffraction was measured by a SMART APEX II X-ray single crystal diffractometers (Bruker AXS, analytical equipment of Krasnoyarsk Center of collective use of SB RAS) equipped

with a CCD-detector, graphite monochromator and Mo K α radiation ($\lambda = 1.5406 \text{ \AA}$) at 80 K.

Phase structure and morphology. The phase structure was measured by XRD (PANalytical Corporation, Netherlands) with Cu K α radiation ($\lambda = 1.5406 \text{ \AA}$), while the textured degree was estimated by the Lotgering method:

$$F_{00l} = \frac{P - P_0}{1 - P_0}, P = \frac{\sum I_{(00l)}}{\sum I_{(hkl)}}, P_0 = \frac{\sum I_{0(00l)}}{\sum I_{0(hkl)}} \quad (1)$$

where I and I_0 are the X-ray intensities of textured and random samples, respectively.

The microstructure WAS characterized by Quanta F250 field-emission scanning electron microscope (FEI, USA). The EBSD technique was employed to measure the distribution of grain orientation of the samples.

The photoluminescence performance. the PL and PLE were performed on an FLS1000 fluorescence spectrophotometer (Edinburgh Instruments Ltd., U. K.).

Photoluminescence quantum efficiency. The photoluminescence quantum yields (PLQYs) was recorded by Hamamatsu Quantaurus-QY Spectrometer (Model C11347-11). The PLQYs was calculated based on the equation: $\eta_{\text{QE}} = I_s / (E_R - E_s)$, in where I_s is the luminescence emission spectra of the sample, E_R is the spectra of the excitation light of the empty integrated sphere, and E_s is the excitation spectra of the excited sample.

RL and X-ray imaging. the corresponding RL spectra were recorded by FLS1000 fluorescence spectrophotometer (Edinburgh Instruments Ltd., U. K.). Scintillator ceramics were closely attached to the circular window of an integrating sphere with an X-ray source (Amptek Mini-X tube with an Ag target and 4 W maximum power output). X-ray imaging were acquired by using a CMOS camera.

MTF measurements. MTF can be used to evaluate the fundamental spatial resolution performance of an imaging system. The spatial resolution can be determined by the spatial frequency value when $\text{MTF} = 0.2$. The MTF curve was calculated by the slanted-edge method.

γ -ray photon counting and energy spectra were obtained with Hamamatsu photomultiplier tube coupled with Ortek shaping amplifier and subsequently to multichannel analyzer MCA8000D. As γ -ray sources were used radioactive isotopes Am^{241} and Cs^{137} .

References

- Chen, Q. *et al.* All-inorganic perovskite nanocrystal scintillators. *Nature* **561**, 88-93 (2018).
- Ou, X. *et al.* High-resolution X-ray luminescence extension imaging. *Nature* **590**, 410-415 (2021).
- Rowlands, J. A. Material change for X-ray detectors. *Nature* **550**, 47-48 (2017).
- Wang, X. *et al.* Organic phosphors with bright triplet excitons for efficient X-ray-excited luminescence. *Nature Photonics* **15**, 187-192 (2021).
- Xu, X. *et al.* Halide perovskites: A dark horse for direct X-ray imaging. *EcoMat* **2**, e12064 (2020).
- Li, M. & Xia, Z. Recent progress of zero-dimensional luminescent metal halides. *Chem. Soc. Rev.* **50**, 2626-2662 (2021).

7. Lian, L. *et al.* Efficient and Reabsorption-Free Radioluminescence in $\text{Cs}_3\text{Cu}_2\text{I}_5$ Nanocrystals with Self-Trapped Excitons. *Advanced Science* **7**, 2000195 (2020).
8. Yang, B. *et al.* Lead-Free Halide Rb_2CuBr_3 as Sensitive X-Ray Scintillator. *Advanced Materials* **31**, 1904711 (2019).
9. Zhu, W. *et al.* Low-dose real-time X-ray imaging with nontoxic double perovskite scintillators. *Light: Science & Applications* **9**, 112 (2020).
10. Xu, L.-J., Lin, X., He, Q., Worku, M. & Ma, B. Highly efficient eco-friendly X-ray scintillators based on an organic manganese halide. *Nature Communications* **11**, 4329 (2020).
11. Zhang, M. *et al.* Metal Halide Scintillators with Fast and Self-Absorption-Free Defect-Bound Excitonic Radioluminescence for Dynamic X-Ray Imaging. *Advanced Functional Materials* **31**, 2007921 (2021).
12. Huang, P. *et al.* Nano Wave Plates Structuring and Index Matching in Transparent Hydroxyapatite-YAG: Ce Composite Ceramics for High Luminous Efficiency White Light-Emitting Diodes. *Adv. Mater.* **32**, 1905951 (2020).
13. Cho, S. *et al.* Hybridisation of perovskite nanocrystals with organic molecules for highly efficient liquid scintillators. *Light: Science & Applications* **9**, 156 (2020).
14. Jiang, T. *et al.* Highly Efficient and Tunable Emission of Lead-Free Manganese Halides toward White Light-Emitting Diode and X-Ray Scintillation Applications. *Adv. Funct. Mater.* **31**, 2009973 (2021).
15. Ma, W. *et al.* Highly Resolved and Robust Dynamic X-Ray Imaging Using Perovskite Glass-Ceramic Scintillator with Reduced Light Scattering. *Adv. Sci.* **n/a**, 2003728 (2021).
16. Ma, X. *et al.* Pressureless glass crystallization of transparent yttrium aluminum garnet-based nanoceramics. *Nature Communications* **9**, 1175 (2018).
17. Hu, T. *et al.* Glass crystallization making red phosphor for high-power warm white lighting. *Light-Sci. Appl.* **10**, 56 (2021).
18. Apetz, R. & van Bruggen, M. P. B. Transparent Alumina: A Light-Scattering Model. *J. Am. Ceram. Soc.* **86**, 480-486 (2003).
19. Allix, M. *et al.* Highly Transparent BaAl_4O_7 Polycrystalline Ceramic Obtained by Full Crystallization from Glass. *Adv. Mater.* **24**, 5570-5575 (2012).
20. Qiu, C. *et al.* Transparent ferroelectric crystals with ultrahigh piezoelectricity. *Nature* **577**, 350-354 (2020).
21. Guo, J. *et al.* Cold Sintering: Progress, Challenges, and Future Opportunities. *Annu. Rev. Mater. Res.* **49**, 275-295 (2019).
22. Mao, L., Guo, P., Wang, S., Cheetham, A. K. & Seshadri, R. Design Principles for Enhancing Photoluminescence Quantum Yield in Hybrid Manganese Bromides. *J. Am. Chem. Soc.* **142**, 13582-13589 (2020).
23. Xu, L.-J., Sun, C.-Z., Xiao, H., Wu, Y. & Chen, Z.-N. Green-Light-Emitting Diodes based on Tetrabromide Manganese(II) Complex through Solution Process. *Adv. Mater.* **29**, 1605739 (2017).
24. Su, B. *et al.* Mn^{2+} -Doped Metal Halide Perovskites: Structure, Photoluminescence, and Application. *Laser Photonics Rev.* **15**, 2000334 (2021).
25. Rodríguez-Lazcano, Y., Nataf, L. & Rodríguez, F. Electronic structure and luminescence of $[(\text{CH}_3)_4\text{N}_2\text{MnX}_4]$ ($\text{X} = \text{Cl}, \text{Br}$) crystals at high pressures by time-resolved spectroscopy: Pressure effects on the Mn-Mn exchange coupling. *Phys. Rev. B* **80**, 085115 (2009).
26. Zhou, G. *et al.* Unraveling the Near-Unity Narrow-Band Green Emission in Zero-Dimensional Mn^{2+} -Based Metal Halides: A Case Study of $(\text{C}_{10}\text{H}_{16}\text{N})_2\text{Zn}_{1-x}\text{Mn}_x\text{Br}_4$ Solid Solutions. *The Journal of Physical Chemistry Letters* **11**, 5956-5962 (2020).
27. Li, J. *et al.* Grain-orientation-engineered multilayer ceramic capacitors for energy storage applications. *Nat. Mater.* **19**, 999-1005 (2020).
28. Yang, S. *et al.* Textured ferroelectric ceramics with high electromechanical coupling factors over a broad temperature range. *Nat. Commun.* **12**, 1414 (2021).
29. Li, P. *et al.* Ultrahigh Piezoelectric Properties in Textured $(\text{K},\text{Na})\text{NbO}_3$ -Based Lead-Free Ceramics. *Adv. Mater.* **30**, 1705171 (2018).
30. Ohashi, Y., Yasui, N., Yokota, Y., Yoshikawa, A. & Den, T. Submicron-diameter phase-separated scintillator fibers for high-resolution X-ray imaging. *Applied Physics Letters* **102**, 051907 (2013).
31. Daneshi, I. & Mohammadzadeh, M. Design and fabrication of a $\text{CsI}(\text{Tl})$ micro-columnar structure scintillation film for digital dental radiography application. *J. Instrum.* **14**, 10039 (2019).
32. Yang, B. *et al.* Heteroepitaxial passivation of $\text{Cs}_2\text{AgBiBr}_6$ wafers with suppressed ionic migration for X-ray imaging. *Nat. Commun.* **10**, 1989 (2019).
33. Wei, H. *et al.* Sensitive X-ray detectors made of methylammonium lead tribromide perovskite single crystals. *Nat. Photonics* **10**, 333-339 (2016).
34. Wei, W. *et al.* Monolithic integration of hybrid perovskite single crystals with heterogenous substrate for highly sensitive X-ray imaging. *Nat. Photonics* **11**, 315-321 (2017).
35. Zhang, M. *et al.* Oriented-Structured CsCu_2I_3 Film by Close-Space Sublimation and Nanoscale Seed Screening for High-Resolution X-ray Imaging. *Nano Letters* **21**, 1392-1399 (2021).
36. Heo, J. H. *et al.* High-Performance Next-Generation Perovskite Nanocrystal Scintillator for Nondestructive X-Ray Imaging. *Adv. Mater.* **30**, 1801743 (2018).
37. Moghiseh, M. *et al.* Discrimination of Multiple High-Z Materials by Multi-Energy Spectral CT—A Phantom Study. *JSM Biomed Imaging Data Paper* **3**, 1007 (2016).
38. He, Y. *et al.* CsPbBr_3 perovskite detectors with 1.4% energy resolution for high-energy γ -rays. *Nature Photonics* **15**, 36-42 (2021).
39. Ahn, B. J. & Hahn, C. H. Analysis of Pulse Height Distributions of a Gas Electron Multiplier Detector by Using Cs-137 and Sr-90 Radioactive Sources. *Journal of the Korean Physical Society* **73**, 26-32 (2018).
40. Zhou, G. *et al.* Manipulation of Cl/Br transmutation in zero-dimensional Mn^{2+} -based metal halides toward tunable photoluminescence and thermal quenching behaviors. *J. Mater. Chem. C* **9**, 2047-2053 (2021).

Corresponding Author

* xiazg@scut.edu.cn (Z. Xia)

Notes

The authors declare no competing financial interest.

Acknowledgement

This research was supported by the National Natural Science Foundations of China (Grant No. 51972118 and 51961145101), International Cooperation Project of National Key Research and Development Program of China (2021YFE0105700), Guangzhou Science & Technology Project (202007020005), and the Local Innovative and Research Teams Project of Guangdong Pearl River Talents Program (2017BT01X137). M.V.K. acknowledges financial support from ETH Zurich through the ETH+ Project SynMatLab ("Laboratory for Multiscale Materials Synthesis") and from the European Union through Horizon 2020 (ERC Consolidator Grant SCALE-HALO, grant agreement No. [819740])

Author contributions

Z.G.X. initiated and guided the research. K.H. synthesized, characterized the samples and wrote the manuscript, and Z.G.X, M.V.K. and Q.Y.Z. revised it. K.H., K.S. and J.C.J interpreted

the theoretical and experimental results. M.V.K. and K.S. characterized detector performance. All authors discussed the results and commented on the manuscript.